Supplementary Information (SI) for Journal of Materials Chemistry C.

Supplementary Information

Combinatorial synthesis and characterization of thin film $Al_{1-x}RE_xN$ (RE = Pr^{3+} and Tb^{3+}) heterostructural alloys

Binod Paudel,*[a,b] John S. Mangum,[b] Christopher L. Rom,[b] Kingsley Egbo,[b] Cheng-Wei Lee,[a,b] Harvey Guthrey,[b] Sean Allen,[b] Nancy M. Haegel,[b] Keisuke Yazawa,[a,b] Geoff L. Brennecka[a] and Rebecca W. Smaha*[b]

[a]*Department of Metallurgical and Materials Engineering, Colorado School of Mines, Golden, CO 80401, USA*

[b]*National Renewable Energy Laboratory, Golden, CO 80401, USA*

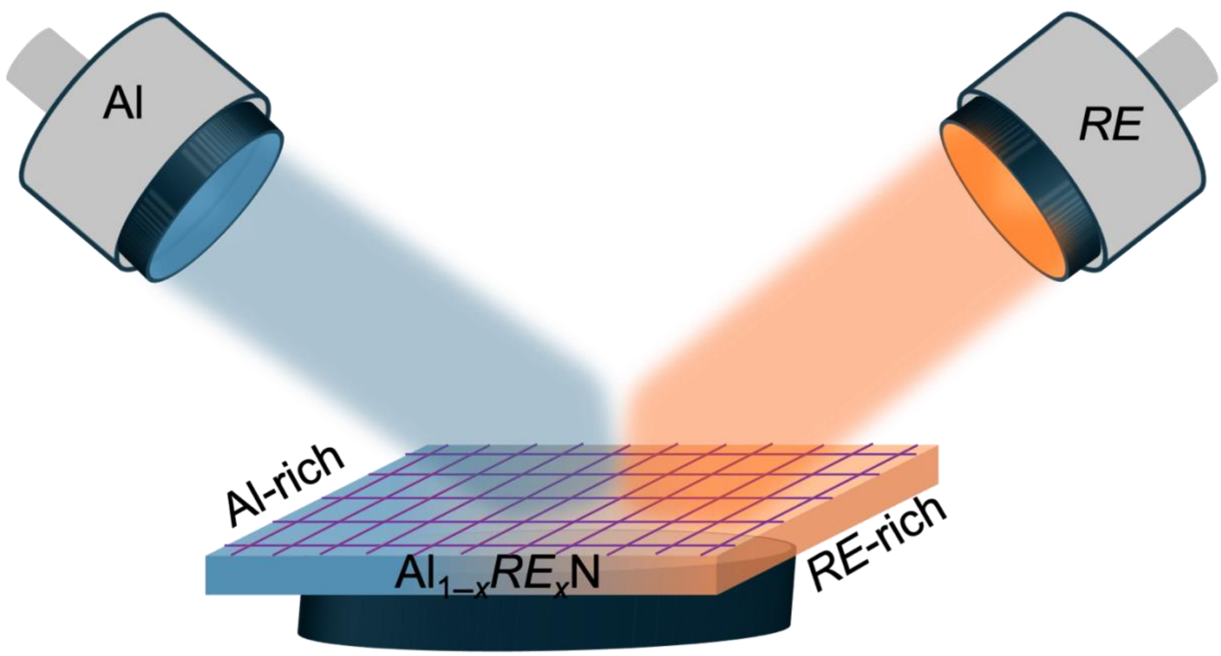

Figure S1: Magnetron sputtering schematic for the high throughput combinatorial synthesis showing a compositional gradient from Al-rich to *RE*-rich regions of the film.

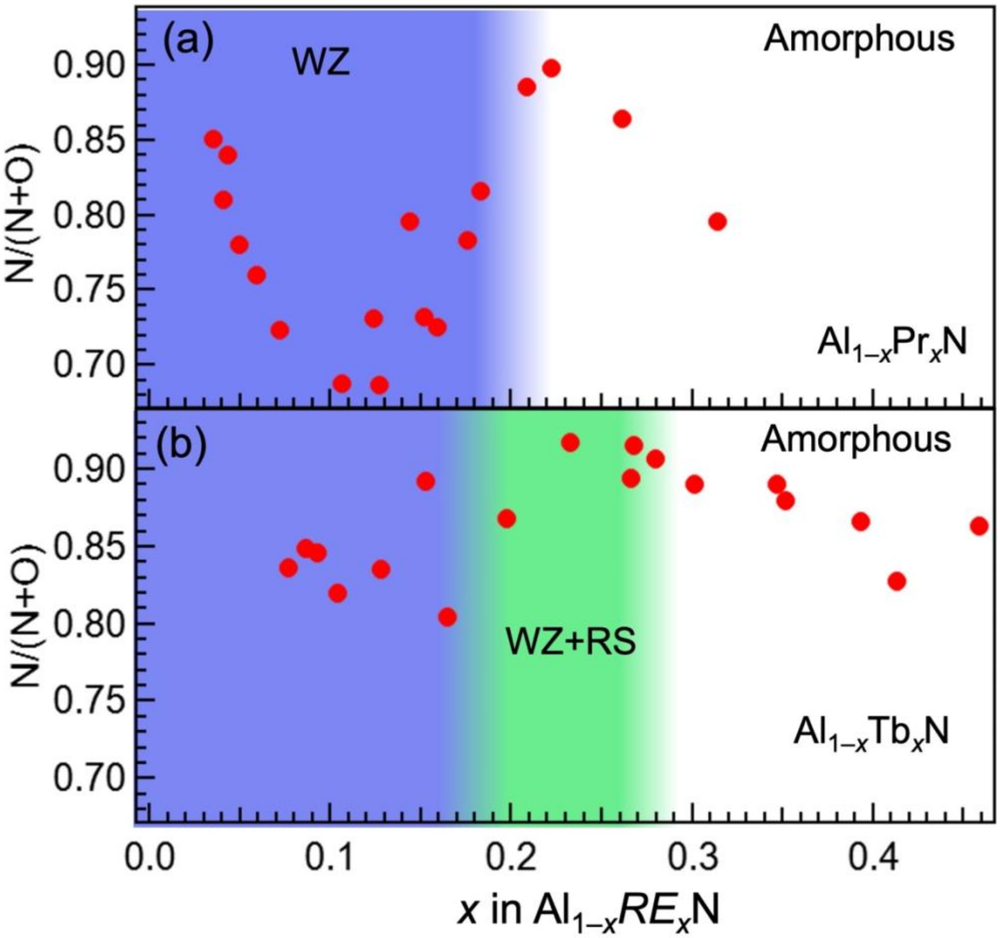

Figure S2: (a,b) Nitrogen composition vs. *RE* composition (x) measured with EPMA for (a) $Al_{1-x}Pr_xN$ and (b) $Al_{1-x}Tb_xN$ films across all detected phases.

Table S1: Comparison of overall stoichiometry and nitrogen composition extracted from STEM-EDS and EPMA

	EDS (near substrate)	EDS (surface)	EPMA
$Al_{0.94}Pr_{0.06}N$ N/(N+O)	$Al_{0.94}Pr_{0.06}N_{0.92}O_{0.08}$ 0.92	$Al_{0.94}Pr_{0.06}N_{0.49}O_{0.23}$ 0.68	$Al_{0.94}Pr_{0.06}N_{0.98}O_{0.30}$ 0.76
$Al_{0.85}Pr_{0.15}N$ N/(N+O)	$Al_{0.85}Pr_{0.27}N_{0.87}O_{0.05}$ 0.94	$Al_{0.85}Pr_{0.25}N_{0.91}O_{0.23}$ 0.80	$Al_{0.86}Pr_{0.14}N_{0.97}O_{0.25}$ 0.73
$Al_{0.92}Tb_{0.08}N$ N/(N+O)	$Al_{0.91}Tb_{0.07}N_{0.93}O_{0.04}$ 0.96	$Al_{0.92}Tb_{0.07}N_{0.8}O_{0.15}$ 0.84	$Al_{0.91}Tb_{0.08}N_{0.96}O_{0.17}$ 0.83
$Al_{0.79}Tb_{0.21}N$ N/(N+O)	$Al_{0.75}Tb_{0.23}N_{0.86}O_{0.15}$ 0.85	$Al_{0.76}Tb_{0.2}N_{0.78}O_{0.35}$ 0.68	$Al_{0.76}Tb_{0.23}N_{0.97}O_{0.09}$ 0.90

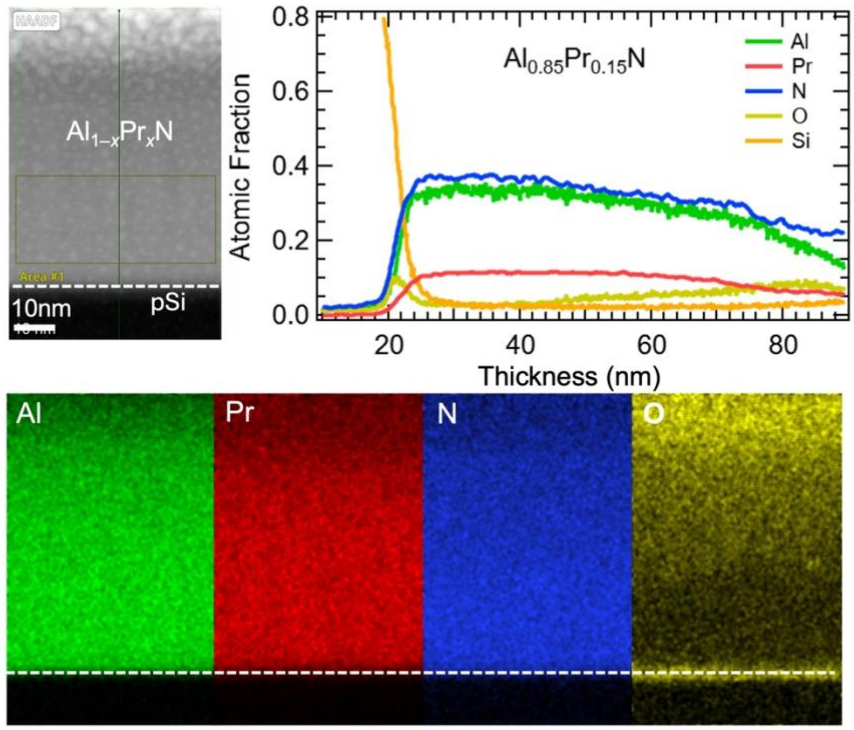

Figure S3: STEM-HAADF image and EDS elemental mapping at the Al *K*-peak, Pr *L*-peak, N *K*-peak, and O *K*-peak for $Al_{0.85}Pr_{0.15}N$ on a pSi substrate, along with the EDS atomic % line profile.

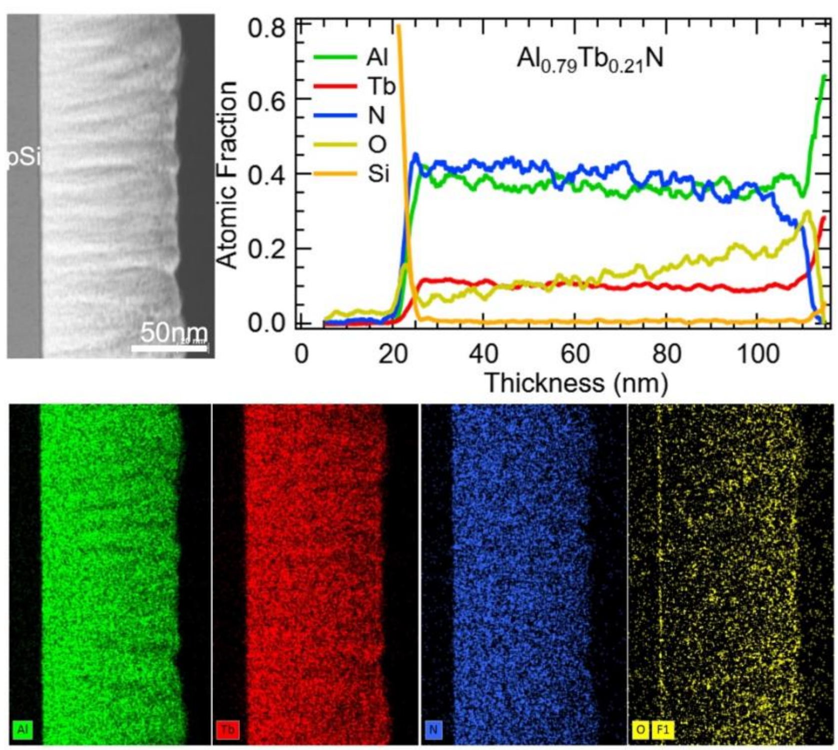

Figure S4: STEM-HAADF image and EDS elemental mapping at the Al *K*-peak, Tb *L*-peak, N *K*-peak, and O *K* peak for $Al_{0.79}Tb_{0.21}N$ on a pSi substrate, along with the EDS atomic % line profile.

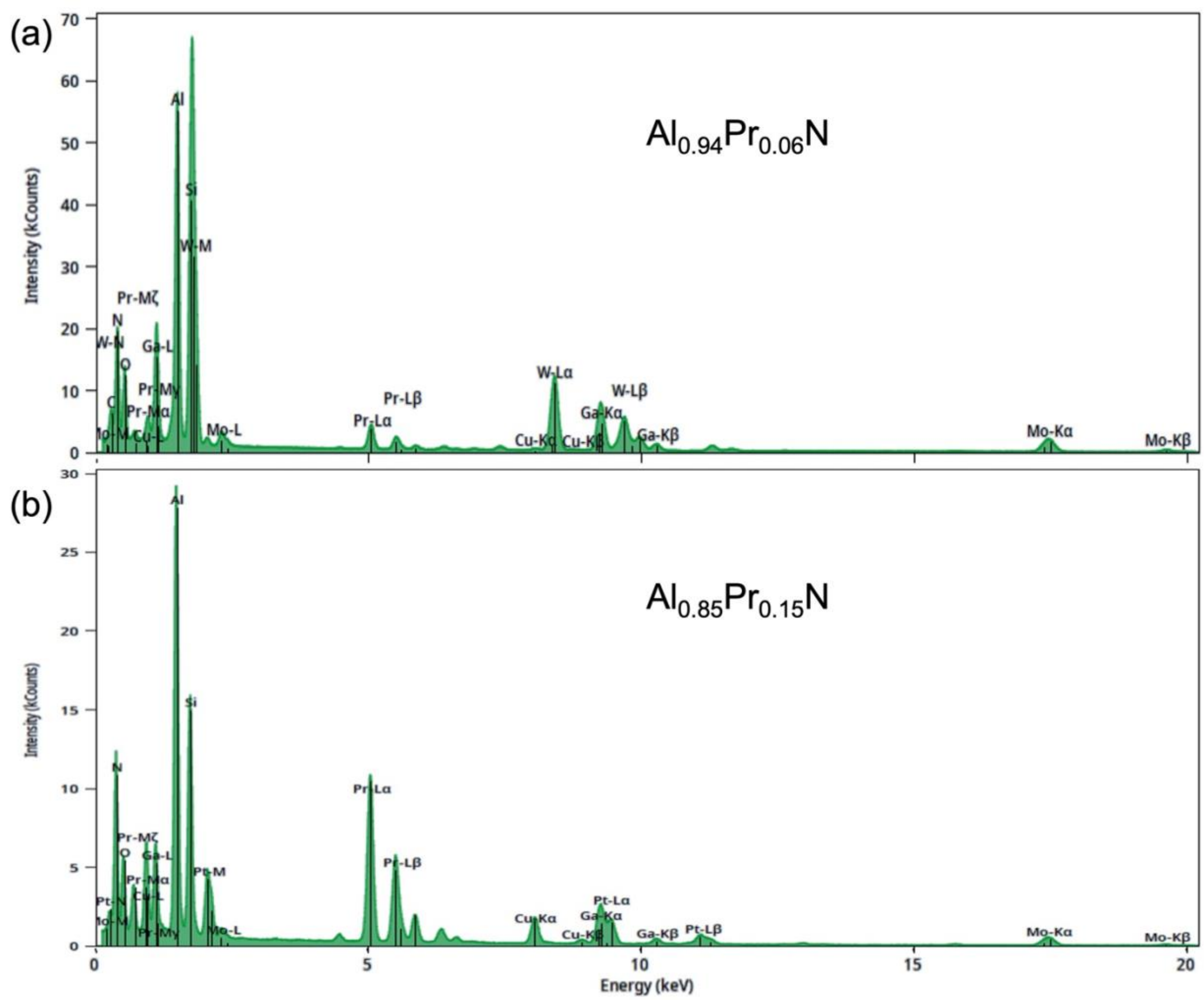

Figure S5: STEM-EDS spectra from (a) $Al_{0.94}Pr_{0.06}N$ and (b) $Al_{0.85}Pr_{0.15}N$ films on pSi substrates, collected over the whole map area. The $Al_{0.94}Pr_{0.06}N$ film was prepared with a W protective layer in the FIB, while Pt was used for the $Al_{0.85}Pr_{0.15}N$ film. Mo and Cu are extraneous signals from the TEM sample holder and Ga is from the FIB processing.

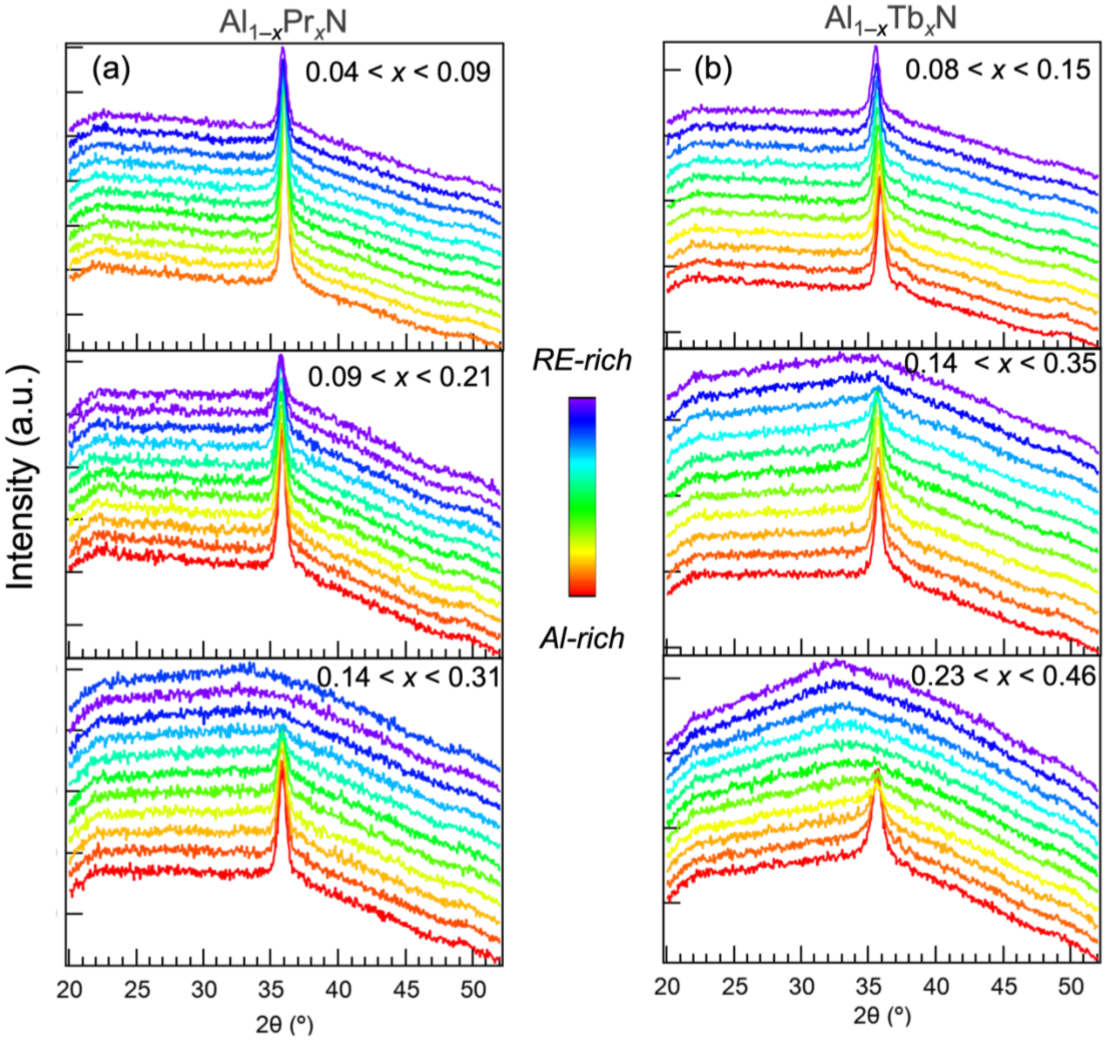

Figure S6: Lab XRD data of (a) $Al_{1-x}Pr_xN$ films with x from 0.04 to 0.31 and (b) $Al_{1-x}Tb_xN$ films with x from 0.08 to 0.46.

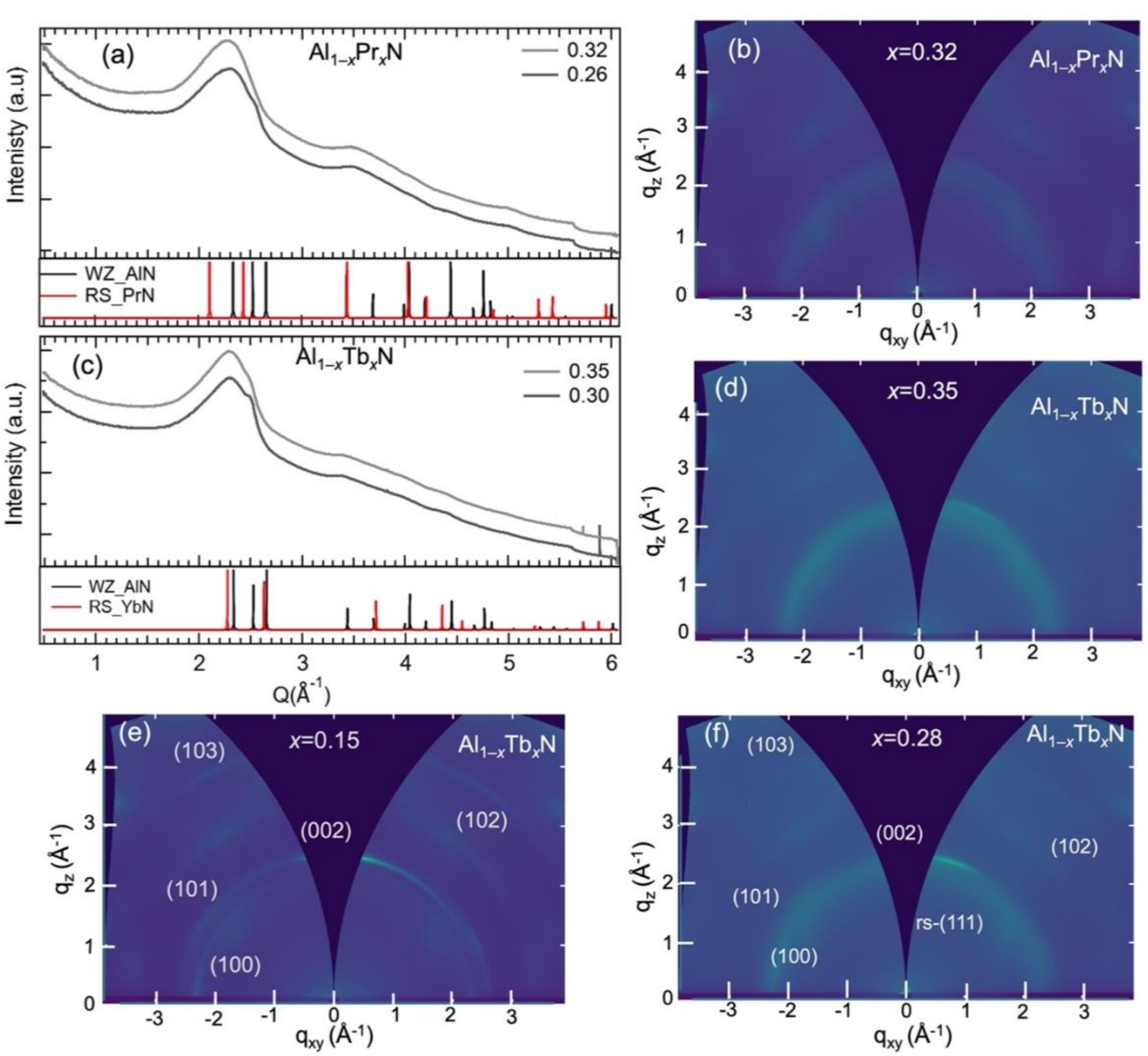

Figure S7: (a,c) Integrated GIWAXS patterns of two amorphous points in (a) $Al_{1-x}Pr_xN$ and (c) $Al_{1-x}Tb_xN$. (b,d) The 2D detector images of one of the amorphous points of (b) $Al_{1-x}Pr_xN$ ($x \approx 0.32$) and (d) $Al_{1-x}Tb_xN$ ($x \approx 0.35$). (e,f) Additional 2D detector images of $Al_{1-x}Tb_xN$ films showing the (e) wz/wz+rs and (f) wz+rs/amorphous boundaries at $x \approx 0.15$ and $x \approx 0.28$ respectively.

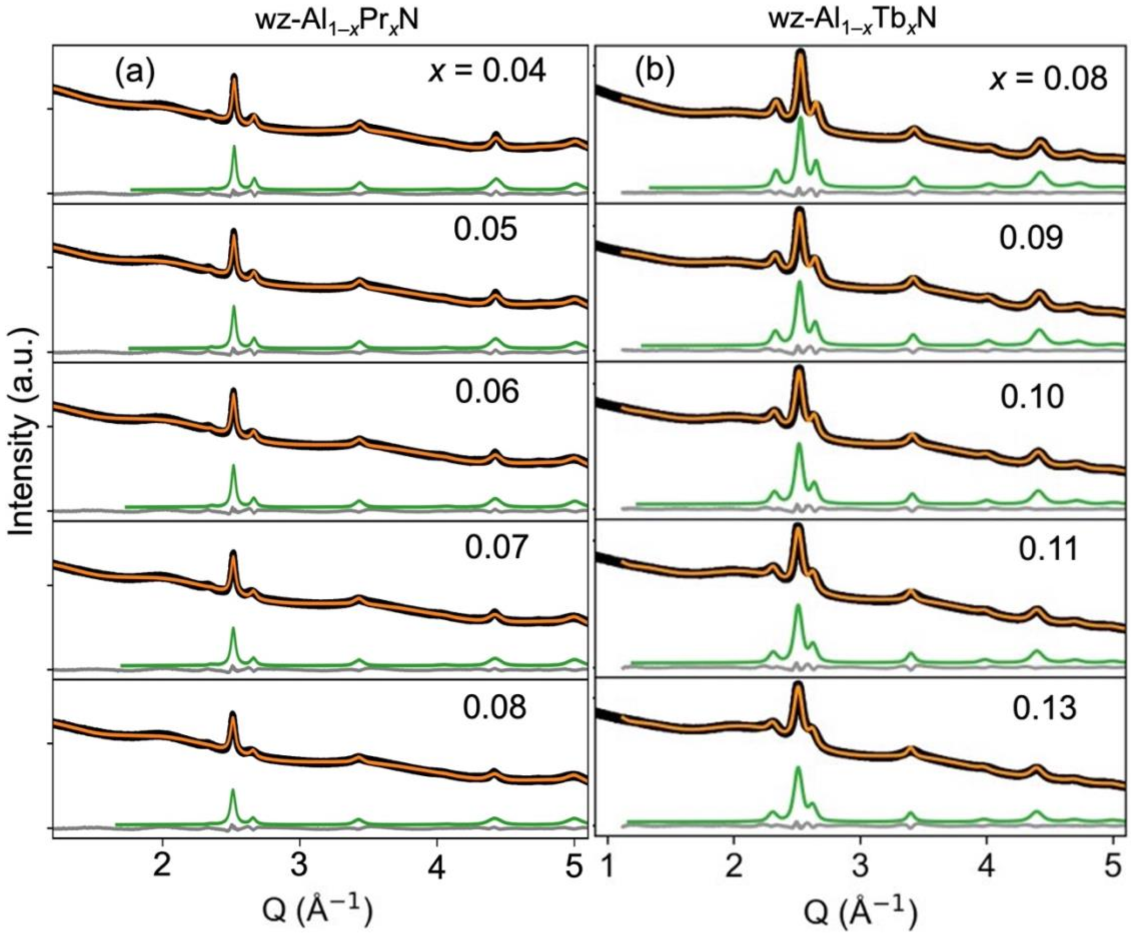

Figure S8: LeBail fits of select GIWAXS data of (a) $Al_{1-x}Pr_xN$ in a phase-pure wurtzite structure with x from 0.04 to 0.08, and (b) $Al_{1-x}Tb_xN$ films in a phase-pure wurtzite structure with up to x≈0.13. Black dots are data, orange traces show overall fit (phase + background), green traces show the fit component from the wz phase, and the gray trace shows the difference between the data and the overall fit.

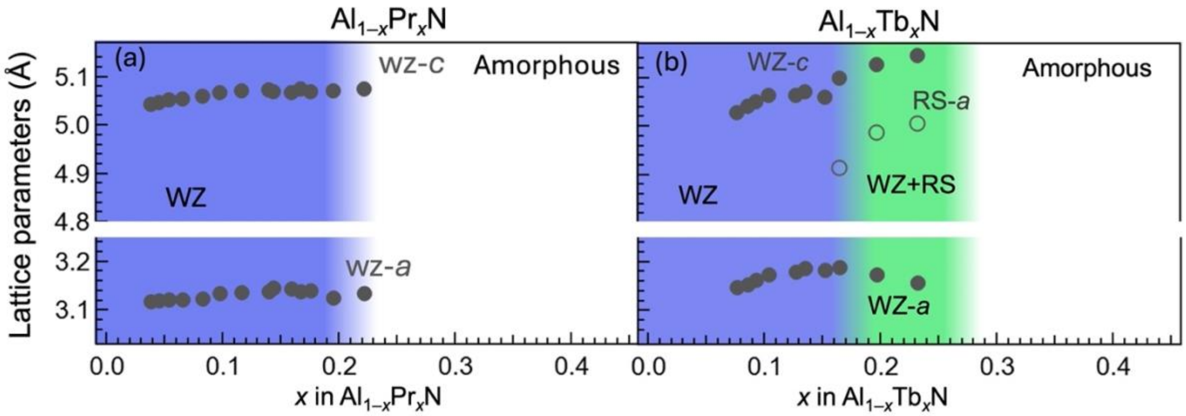

Figure S9: Lattice parameters extracted from LeBail fits of (a) $Al_{1-x}Pr_xN$ films, and (b) $Al_{1-x}Tb_xN$ films. In the phase-pure wurtzite regions of $Al_{1-x}Pr_xN$ (up to x≈0.22) and $Al_{1-x}Tb_xN$ (up to x≈0.14), the wurtzite a and c lattice parameters were extracted. In the mixed wz+rs phase region for $Al_{1-x}Tb_xN$ (0.15≲x≲0.28), both the wurtzite a and c lattice parameters and the rocksalt a lattice parameter were extracted.

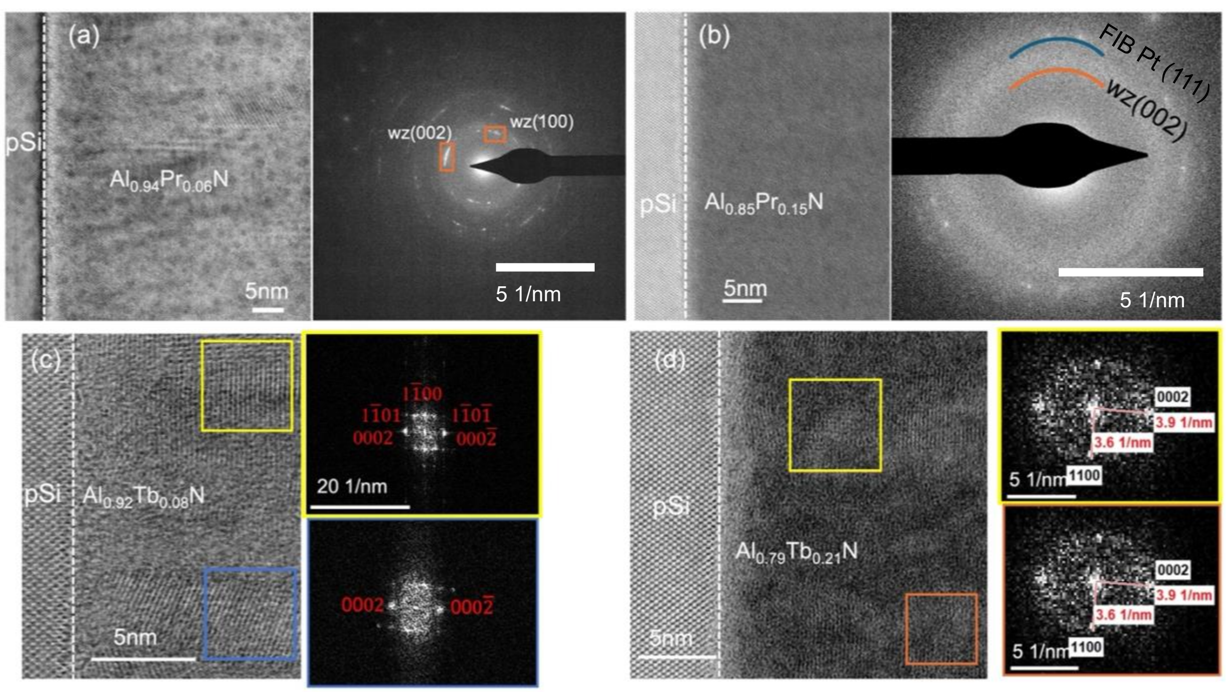

Figure S10: (a,b) STEM-DF images and SAED patterns of $Al_{1-x}Pr_xN$ with (a) x≈0.06 and (b) x≈0.15. For x≈0.06, the SAED shows peaks from the wurtzite phase. For x≈0.15, the SAED shows a diffuse ring that lines up with the (002) d-spacing of the wurtzite phase. The outer ring denoted by the blue arc arises from the nanocrystalline Pt deposited during the FIB process. (c,d) STEM-BF images and fast Fourier transforms (FFTs) at two different regions of each STEM-BF image of $Al_{1-x}Tb_xN$ with (c) x=0.08 and (d) x=0.21. The FFTs indicate the presence of the wurtzite phase.

Table S2: Reference CL peaks of Pr^{3+} compared with those observed in our measurements.

Transition	**Reference Wavelength (nm)**	**Observed wavelength (nm)**
$^3P_0 \rightarrow {}^3H_4$	490	—
$^3P_1 \rightarrow {}^3H_5$	526	527
$^1D_2 \rightarrow {}^3H_4$	603	—
$^3P_0 \rightarrow {}^3F_2$	650	654
$^3P_1 \rightarrow {}^3F_3$	673	673
$^3P_0 \rightarrow {}^3F_3$	694	—
$^1D_2 \rightarrow {}^3H_5$	696	—

Table S3: Reference CL peaks of Tb^{3+} compared with those observed in our measurements.

Transition	**Reference Wavelength (nm)**	**Observed wavelength (nm)**
$^5D_3 \rightarrow {}^7F_6$	384	—
$^5D_3 \rightarrow {}^7F_5$	424	—
$^5D_3 \rightarrow {}^7F_4$	444	—
$^5D_3 \rightarrow {}^7F_3$	463	—
$^5D_3 \rightarrow {}^7F_2$	467	—
$^5D_4 \rightarrow {}^7F_6$	496	492
$^5D_4 \rightarrow {}^7F_5$	551	554
$^5D_4 \rightarrow {}^7F_4$	587	589
$^5D_4 \rightarrow {}^7F_3$	626	627
$^5D_4 \rightarrow {}^7F_2$	660	656